The Bending Feature of the *Fermi* Bubbles: A Presumed Horizontal Galactic Wind and Its Implication on the Bubbles' Age

Guobin Mou[1,2] , Dongze Sun[3], and Fuguo Xie[2]

[1] School of Physics and Technology, Wuhan University, Wuhan 430072, People's Republic of China; gbmou@escience.cn
[2] Key Laboratory for Research in Galaxies and Cosmology, Shanghai Astronomical Observatory,
Chinese Academy of Sciences, 80 Nandan Road, Shanghai 200030, People's Republic of China
[3] HongYi Honor College of Wuhan University, Wuhan 430072, People's Republic of China

Abstract

There are two spectacular structures in our Milky Way: the *Fermi* bubbles in gamma-ray observations and the North Polar Spur (NPS) structure in X-ray observations. Because of their morphological similarities, they may share the same origin, i.e., related to the past activity of Galactic center. These structures demonstrate a significant bending feature toward the west in Galactic coordinates. This inspires us to consider the possibility that the bending may be caused by a presumed global horizontal galactic wind (HGW) blowing from the east to the west. Under this assumption, we adopt a toy shock-expansion model to understand two observational features: (1) the relative thickness of the NPS; (2) the bending of the *Fermi* bubbles and the NPS. In this model, the contact discontinuity marks the boundary of the *Fermi* bubbles, and the shocked interstellar medium (ISM) marks the NPS X-ray structure. We find that the Mach number of the forward shock in the east is $\sim$1.9–2.3, and the velocity of the HGW is $\sim$0.7–0.9c_s. Depending on the temperature of the pre-shock ISM, the velocity of the expanding NPS in Galactic coordinates is around 180–290 km s^{-1}, and the HGW is $\sim$110–190 km s^{-1}. We argue that the age of the NPS and the *Fermi* bubbles is about 18–34 Myr. This is a novel method, independent of injection theories and radiative mechanisms, for the estimation on the age of the *Fermi* bubble/NPS.

Key words: galaxies: active – gamma-rays: galaxies – ISM: jets and outflows – X-rays: galaxies
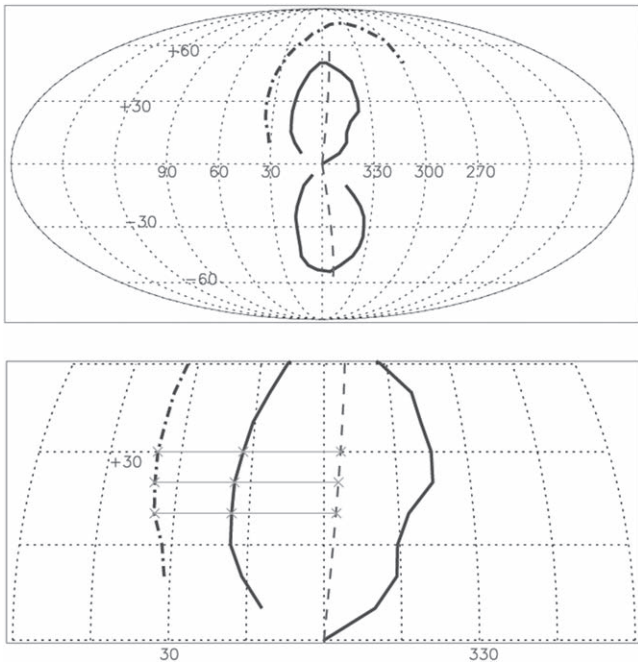
1. Introduction

Two giant gamma-ray bubbles located symmetrically above and below the Galactic plane are revealed by the *Fermi* Gamma-ray Space Telescope (Dobler et al. 2010; Su et al. 2010; Ackermann et al. 2014). Each of the bubbles is roughly $\sim$50° in height and $\sim$40° in width. If the Sun–Galactic center (GC) distance is 8.5 kpc (Ghez et al. 2008), considering the projection effect of a three-dimensional structure, the physical height is 9–10 kpc, while the width is 5–6 kpc (e.g., Guo et al. 2012; Mou et al. 2015; Sarkar 2019). More interestingly, in the X-ray band, the *ROSAT* All-Sky Survey at 1.5 keV showed a giant limb-brightened feature in the northeast sky that is usually called the North Polar Spur (NPS), and a less significant counterpart in the northwest sky that is usually called the NPS-W (Snowden et al. 1997). The distance of the NPS is still under debate: it may be located at the Galactic halo with a distance of several kpc (e.g., Sofue 2000; Kataoka et al. 2013; Sun et al. 2014; Sofue 2015; Lallement et al. 2016; Sofue et al. 2016; Akita et al. 2018), or it may be a local structure near the Sun with a distance of several hundred pc (e.g., Egger & Aschenbach 1995; Wolleben 2007; Puspitarini et al. 2014). However, as is shown in Figure 1, morphologically the NPS structure seems to be located just outside and surrounding the north *Fermi* bubble (NFB), which implies that the two structures may share a common origin (Su et al. 2010).

The formation and radiative mechanism of the *Fermi* bubbles and the NPS structure are still under debate. These structures may either relate to wind driven by star formation in the GC (Crocker & Aharonian 2011; Carretti et al. 2013; Crocker et al. 2014, 2015; Sarkar et al. 2015), or relate to the past activities of supermassive black hole residing in the GC—Sgr A* (Guo & Mathews 2012; Guo et al. 2012; Yang et al.
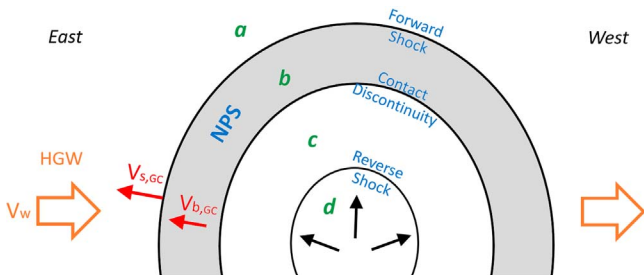
2012, 2013; Zubovas & Nayakshin 2012; Mou et al. 2014, 2015; Yang & Ruszkowski 2017). In those Sgr A*-induced scenarios, it is assumed that Sgr A* has experienced a much more luminous active period (compared to the current dim non-active period) that began millions of years ago (see the review by Totani 2006). During that active period, a huge amount of energy was ejected out, through either collimated jet or un-collimated wind, from the accretion system of Sgr A*. The high-speed outflowing material rushes into the interstellar medium (ISM) in the galactic halo, creating expanding shock structures. In these shock-based scenarios, geometrically the *Fermi* bubble is bounded by the contact discontinuity (CD), while the NPS structure corresponds to the post-shock ISM (see Section 2.2 and the shaded region in the bottom panel of Figure 2 below).

Apart from understanding the morphological structures, there are two possible models for the γ-ray emission of the *Fermi* bubbles: the leptonic model and the hadronic model. The resulting age estimations on the *Fermi* bubbles are very different; these are summarized in Table 1. In the leptonic model, the gamma-ray photons come from inverse Compton (IC) scattering on soft photons (including starlight and cosmic microwave background) by cosmic ray electrons (CRe). Because the cooling timescale of CRe at energies $\sim$1 TeV that demanded fitting the γ-ray SED is shorter than $\sim$1 Myr (Figure 28 in Su et al. 2010), the age of the *Fermi* bubbles should also be shorter than this timescale, demanding a very strong jet power (Guo & Mathews 2012; Guo et al. 2012; Yang et al. 2012, 2013; Yang & Ruszkowski 2017).

In the hadronic model, on the other hand, the gamma-ray photons are generated during the π^0 decays that are produced in collisions between the CR protons (CRPs) and thermal nuclei (so-called *pp* collisions). The cooling timescale of CRPs is

Figure 1. Upper panel: morphologies of the *Fermi* bubbles (solid curve; see Su et al. 2010), and the NPS structure in 1.5 keV band in Galactic coordinates (see Snowden et al. 1997). The dotted–dashed curve masks the outer boundary of the NPS. Both the *Fermi* bubbles and the NPS seem to bend significantly toward the west. The north *Fermi* bubble has a bending angle of $\theta_{\rm bend} \sim 7°$ (dashed curve), while the south bubble has a bending angle of $\sim 11°$ (dashed curve). Bottom panel: zoom-in of the middle part ($b = 0°–45°$, $l = 60° − 0°–300°$) of the upper panel. We show three gray solid lines to measure the thickness of the NPS, and the distance of the outer edge of the NPS to the expansion center. The gray crosses mark the measuring points: expansion center, east edge of the NPS, and the NFB.

Figure 2. Toy shock model for the *Fermi* bubble and NPS structures. The supersonic outflow from the GC interacts with the ambient ISM, forming shock structures. The space can be divided into four zones: (*a*) pre-shock ISM; (*b*) post-shock ISM; (*c*) post-shock outflow; and (*d*) supersonic outflow (Weaver et al. 1977). The outer edge of the NPS is the forward shock front, and the *Fermi* bubble's edge is the CD. We assume a horizontal galactic wind (HGW) blowing from the east to the west, as shown by orange arrows.

$t_{pp} \gtrsim 3.5 \times 10^9$ yr $(0.01 \, {\rm cm}^{-3} n_{\rm H}^{-1})$ (Crocker et al. 2014). Therefore, the hadronic model predicts a much longer age of the *Fermi* bubbles than the leptonic model; e.g., it is around 7–12 Myr in Mou et al. (2014, 2015), or a few hundreds Myr in Crocker et al. (2014, 2015).

In this Letter, we focus on the relative thickness of the NPS and the bending feature of both the *Fermi* bubbles and the NPS. The former feature implies the strength of the forward shock, while the latter may imply the existence of a presumed horizontal galactic wind (HGW). Based on this assumption, we built a toy model to estimate the HGW's velocity, the expanding velocity of NPS (east side), and the age of the

Fermi bubbles. In Section 2 we present the observations of the *Fermi* bubbles and the NPS. Then we present our model, including its key assumptions and the corresponding calculations. This provides a novel method, independent of injection theories (i.e., accretion-driven jet, accretion-driven wind, or star-formation-driven wind) and radiative mechanisms (leptonic or hadronic) for the age estimation. We briefly discuss our results in Section 3.

2. Our Model and Results

2.1. Morphological Information of the NPS and the Fermi Bubbles

In Figure 1 we plot the morphologies of the NPS in the 1.5 keV band (Snowden et al. 1997) and the *Fermi* bubbles (solid curve; Su et al. 2010). Evidently, both the NPS and the *Fermi* bubbles seem to bend toward the west. The bending angle is about $\theta_{\rm bend} \approx 6°–8°$ for the NFB. The X-ray observations also indicate that the NPS-W is fainter than the NPS (not shown here, see Snowden et al. 1997). The asymmetric morphologies imply that they probably suffered from a presumed HGW in the halo blowing from the east to the west.

Another result from this figure is that we can measure the ratio between the thickness of the NPS ($\Delta R_{\rm NPS}$) and the distance from the outer boundary of the NPS structure to the expansion center ($d_{\rm NPS}$). Such information will later be used to determine the Mach number of the forward shock. From the zoom-in plot (bottom panel of Figure 1), we can estimate the distance between the east edge of the NPS or the NFB and the expansion center. The formula is

$$d_{\rm NPS,NFB} = \frac{d_\odot \sin(l_1 − l_2)}{\cos(b)\cos(l_2)} \qquad (1)$$

in which $d_\odot = 8.5$ kpc, b is the latitude of measuring points, and l_1 and l_2 are the longitude of the east edge of NPS/NFB and the expansion center (EC), respectively (see gray crosses plotted in the bottom panel of Figure 1). Our results are shown in Table 2.

2.2. Our Toy Model

Our toy model is based on three assumptions. First, the *Fermi* bubbles and the NPS share a common origin, related to the past activities of the GC. Second, there exists a global east-to-west blowing HGW in the Galactic halo, which bends the *Fermi* bubbles and the NPS by degrees toward the west. Third, we assume that the nucleus activity is a constant over time. We note that if the density of the ISM follows the observed form $n_e \propto r^{−2.1}$ in Miller & Bregman (2013), the velocity of the forward shock virtually does not change with time for a constant injected power, based on analytical solutions of the shock's evolution (see Equation (9) in Mou et al. 2014).

Now we provide more details of our toy model. The schematic diagram is shown in Figure 2. The supersonic outflow is injected from the GC. The outflow may be in the form of star-formation-driven wind in the central regions of our galaxy, jet, wind from a quasar state accretion disk, or wind from hot accretion disk (see Yuan & Narayan 2014; Yuan et al. 2015 for hot accretion wind). The exact form of the outflow is irrelevant for the investigations here. As shown in Figure 2, shock structures are generated by the supersonic outflow. The

Table 1
Theoretical Models for the *Fermi* Bubbles

Dynamical Model	Injected Outflow Velocity	Total Injected Energy	Radiation Model	τ_{Fermi} (Myr)
Jet[a]	$V_{jet} = 0.1$ c	$\sim 10^{56-57}$ erg	leptonic	1–2
Jet[b]	$V_{jet} = 0.025$ c	$\sim 10^{57}$ erg	leptonic	~ 1
Quasar wind[c]	$V_{wind} = 0.1$ c	$\sim 10^{57}$ erg	leptonic	~ 6
Hot accretion wind[d]	$V_{wind} \simeq 0.05$ c	$\sim 10^{55-56}$ erg	hadronic dominated	7–12
Star-formation-driven wind[e]	$V_{wind} \simeq 1000$ km s^{-1}	$\sim 10^{55-57}$ erg	hadronic	200–10^3
Star-formation-driven wind[f]	$V_{wind} \simeq 1000$ km s^{-1}	$\sim 10^{55}$ erg	leptonic	30

Notes.
[a] References: Guo & Mathews (2012), Guo et al. (2012).
[b] Ref: Yang et al. (2012, 2013), Yang & Ruszkowski (2017).
[c] Ref: Zubovas et al. (2011), Zubovas & Nayakshin (2012).
[d] Ref: Mou et al. (2014, 2015).
[e] Ref: Crocker & Aharonian (2011), Crocker et al. (2014, 2015).
[f] Ref: Sarkar et al. (2015), Sarkar (2019).

ram pressure of the supersonic outflow is balanced by the thermal pressure of the post-shock outflow gas (region *c*) at the reverse shock front. The interface between the post-shock outflow (region *c*) and the post-shock ISM (region *b*) is called the CD.

The boundary of the *Fermi* bubbles is generally determined by the CD, because the magnetic field in the post-shock ISM is parallel to the CD, which can bound the CRs inside of the CD (Yang et al. 2012), or outside but close to the CD (Mou et al. 2015). According to simulations of jet/quasar wind/hot accretion wind models, across the CD from region *c* to region *b*, there is a sharp increase in density and a sharp decrease in temperature. The forward shock front compresses the ISM, making a hotter and denser post-shock ISM (region *b*) compared to the pre-shock ISM (region *a*). Thus the shocked ISM (region *b*) will be the brightest in the X-ray band among regions *a*–*c*, likely corresponding to the NPS structure surrounding the north *Fermi* bubble (Su et al. 2010). Such a scenario is adopted in almost all of the models mentioned above.

If there is an "east-to-west" blowing HGW, both the *Fermi* bubbles and the NPS bend toward the west. The Mach number of the eastern forward shock will be larger than that of its western counterpart. Consequently, the density and temperature in the eastern post-shock ISM would be higher than those in the western post-shock ISM. Consequently, the NPS in the east will be brighter than the NPS-W in the X-ray image, a phenomenon that has already been observed. A reliable measurement of the thickness of the NPS can be made in the east because of its clear image.

The rationality of the existence of the HGW may be controversial. In addition to the two aspects mentioned above, we here add some more arguments. First, according to *ROSAT* X-ray observations, in the northern galactic hemisphere, the outflows close to the GC are perpendicular to the galactic plane (Figure 19. in Su et al. 2010, also see Zubovas & Nayakshin 2012 for simulations on interactions between quasar outflows and massive Central Molecular Zone in the GC). However, the NPS/*Fermi* bubble caused by outflow is significantly bending toward the west in a higher latitude. Therefore, we believe that the bending is most likely due to HGW, not for other reasons. Second, head-tail radio galaxies are very common, in which jets appear to be bent by ram pressure. Those wind velocities range from a few hundred to several thousand kilometers per second (e.g., see Table 5 in

O'Donoghue et al. 1993). In our Local Group, M31 ($l = 121°$, $b = -22°$, roughly east in Galactic coordinates) is approaching us at 110 km s^{-1}. Galaxies are not stationary in the group, and the proper motions of the galaxies and gas can more or less produce winds. Therefore we posit that the existence of such a wind is not unreasonable.

2.3. The Relative Thickness of NPS

With subscript "1" representing the east part, the shock velocity in the frame of pre-shock ISM, i.e., $V_{s,1}$, can be written as

$$V_{s,1} = V_{s,GC} + V_w = M_1 c_s, \quad (2)$$

and the velocity of the CD in this frame is

$$V_{cd,1} = V_{cd,GC} + V_w, \quad (3)$$

where $V_{s,GC}$ is the velocity of the forward shock in the GC frame, V_w is the HGW velocity in the GC frame, c_s is the adiabatic sound speed of the pre-shock ISM, M_1 is the Mach number of the forward shock, and $V_{cd,GC}$ is the velocity of the contact discontinuity in the frame of the GC.

We first use the ratio between the thickness of the NPS (ΔR_{NPS}) and the distance from the outer boundary of this structure to the expansion center (d_{NPS}), i.e.,

$$f_1 \equiv \frac{\Delta R_{NPS}}{d_{NPS}} = \frac{V_{s,GC} - V_{cd,GC}}{V_{s,GC}} = \frac{r_t(M_1)}{1 - V_w/(M_1 c_s)}, \quad (4)$$

where $r_t(M_1) \equiv (V_{s,1} - V_{cd,1})/V_{s,1}$ is the relative thickness of the shocked ISM in HGW's frame, and $r_t(M_1)$ is mainly determined by the Mach number M_1 (see below for the relationship). The range of f_1 depends on the bending angle and measuring points, and ranges from 0.391 to 0.443 (Table 2). The sound speed of unshocked gas in galactic halo c_s is determined by observations, in which the temperature of galactic halo is estimated to be $T = 1$–2×10^6 K (Kuntz & Snowden 2000; Miller & Bregman 2013, 2016; Sofue et al. 2018). Therefore, the sound speed c_s is 150–210 km s^{-1} as $c_s^2 = \gamma k_B T/(\mu m_H)$, in which $\mu = 0.63$ for solar abundances.

We have made numerical simulations to find the relationship between M_f and r_t (M_f is the forward shock's Mach number, and r_t is the relative thickness defined as the ratio between the thickness of the shocked ISM and forward shock's radius). We use the ZEUSMP code (Stone & Norman 1992; Hayes et al.

Table 2
Results of Measurement on NPS and the NFB

b	l_1–(Long. of NPS)	l_1–(Long. of NFB)	l_2–Long. of EC[a]	d_{NPS}[b]	d_{NFB}[c]	f_1[d]
20°	33°9	18°5	−2°1/−2°5/−2°9	5.32/5.37/5.43	3.18/3.24/3.30	0.401/0.396/0.391
25°	34°7	18°3	−2°6/−3°0/−3°4	5.69/5.74/5.80	3.35/3.41/3.47	0.411/0.406/0.401
30°	35°0	17°0	−3°1/−3°6/−4°1	6.06/6.13/6.21	3.38/3.46/3.54	0.443/0.436/0.429

Notes.
[a] Longitude of the EC, when the bending angle equals 6°, 7°, or 8°.
[b] Distance from east edge of the NPS to expansion center, when the bending angle equals 6°, 7°, or 8°.
[c] Distance from east edge of the NFB to the EC.
[d] Relative thickness: $(d_{NPS} - d_{NFB})/d_{NPS}$.

2006), and choose a 2.5 dimensional Spherical coordinate by assuming that it is symmetric in ϕ-direction. The scale of r-direction is set as 0.1–10 kpc, and it is divided into 900 uniform grids with $dr(i+1)/dr(i) = 1.005$. The initial ISM is assumed to be isothermal, and follows a $\rho_{ISM} \propto r^{-2}$ law, while the gravitational potential is $\Phi = -2\sigma^2/r$ ($\sigma = 124$ km s^{-1}). We inject an isotropic outflow of a certain power at the inner boundary each time, and analyze the evolution of the shock structures. For the initial density obeying r^{-2} law, we can obtain shock structures evolving linearly with time (i.e., the velocities of the forward shock and CD remain constant over time). Our results are plotted in Figure 3, in which Mach numbers cover a range of 1.24–10. We fit the $M_f - r_t$ relationship with an analytical expression:

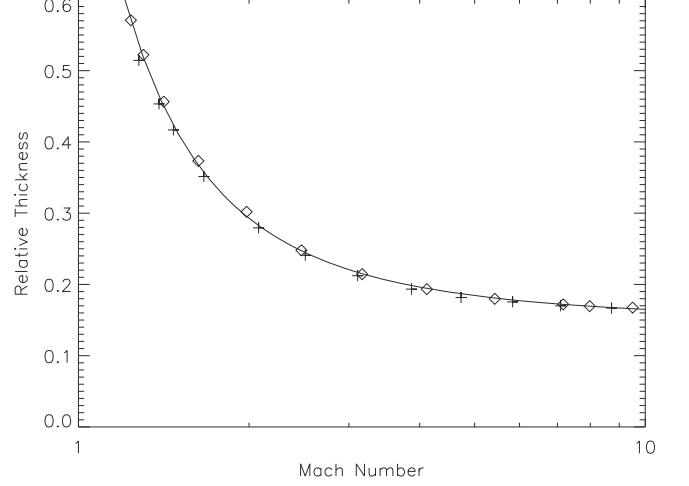$$3/M_f = \ln(r_t - 0.11) + 3.2. \tag{5}$$

In this work, M_f is M_1 mentioned above. According to the $M_f - r_t$ relationship, if there is no HGW or if $V_w/(M_1 c_s)$ is small, then M_1 is $1.43 \sim 1.55$ because $r_t = f_1$ in this case, while if $V_w/(M_1 c_s)$ is not negligible, then M_1 should be larger than this range.

2.4. The Bending of Fermi Bubbles

We then make use of the bending angle of the north Fermi bubble. The bending of a jet in a cross wind has been studied for decades (Burns et al. 1979; Jones & Owen 1979; O'Donoghue et al. 1993), and the bending formula is

$$\rho_{out} \frac{v_{out}^2}{l_{bend}} \sim \rho_0 \frac{V_w^2}{l_{press}} \tag{6}$$

in which ρ_{out} and v_{out} are the density and velocity of outflows (jets or winds launched from the GC in different models), l_{bend} is the radius of the curvature, l_{press} is the length scale over which the ram pressure acts, and ρ_0 is the density of pre-shock gas in galactic halo. Here $l_{bend} \sim H_{FB}/2\theta$, and $l_{press} \sim D_{FB}$ (H_{FB} and D_{FB} are the height and width of Fermi bubbles, respectively). Regarding the projection effect of a three-dimensional structure, we consider three physical lengths of NFB based on simulation works: $(H_{FB}, D_{FB}) = (9 \text{ kpc}, 4.5 \text{ kpc})$ in Sarkar (2019), (9.4 kpc, 5 kpc) in Mou et al. (2015), and (10 kpc, 6 kpc) in Guo et al. (2012). Then $f_2 \equiv l_{bend}/l_{press} = 6.0 \sim 9.6$. Inside of the shock structure, the ram pressure of supersonic outflows is comparable to the thermal pressure of the shocked ISM: $\rho_{out} v_{out}^2 = \Lambda P_b$, in which $\Lambda \sim 1$.

Figure 3. Relationship between the forward shock's Mach number M_f and relative thickness r_t. Crosses mark the simulation results with $\rho_{out}(r_{in}) = 0.1 m_H$ cm^{-3}, diamonds mark the results with $\rho_{out}(r_{in}) = 10.0 m_H$ cm^{-3} ($r_{in} = 0.1$ kpc). The solid line shows the fitting curve (Equation (5)). Although there are two orders of magnitude difference in outflow densities, the $M_f - r_t$ relationships in both cases are highly consistent.

Regarding the Rankine–Hugoniot conditions at the forward shock front in the HGW frame, we have

$$\rho_0 V_{s,1} = \rho_{b,1}(V_{s,1} - V_{b,1}), \tag{7}$$

$$\frac{1}{\gamma}\rho_0 c_s^2 + \rho_0 V_{s,1}^2 = \frac{1}{\gamma}\rho_{b,1}c_{s,1}^2 + \rho_{b,1}(V_{s,1} - V_{b,1})^2, \tag{8}$$
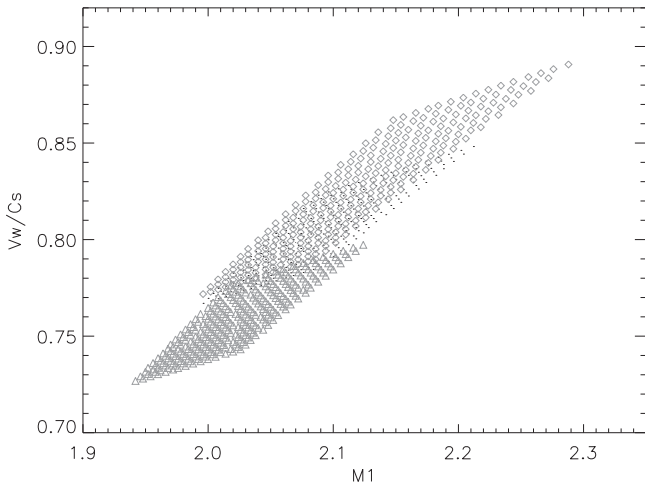
$$\frac{1}{2}V_{s,1}^2 + \frac{5c_s^2}{2\gamma} = \frac{1}{2}(V_{s,1} - V_{b,1})^2 + \frac{5c_{s,1}^2}{2\gamma}. \tag{9}$$

in which $\rho_{b,1}$ and $c_{s,1}$ are the density and sound speed of the post-shock ISM (east part), respectively. With adiabatic index $\gamma = 5/3$, we have $\rho_{b,1} = \rho_0\, 4M_1^2/(M_1^2 + 3)$ and $c_{s,1}^2 = c_s^2(0.3125M_1^2 + 0.875 - 0.1875/M_1^2)$. Therefore, the thermal pressure of post-shock ISM

$$P_b = \rho_{b,1}c_{s,1}^2/\gamma = \rho_0 c_s^2 \frac{3.75M_1^4 + 10.5M_1^2 - 2.25}{5M_1^2 + 15}. \tag{10}$$

With Equations (6) and (10), we finally obtain

$$V_w^2 = c_s^2 \frac{3.75M_1^4 + 10.5M_1^2 - 2.25}{f_2(5M_1^2 + 15)}. \tag{11}$$

Figure 4. Solutions of V_w and c_s according to the range of f_1 and f_2 in the cases of a bending angle that equals 6° (gray triangles), 7° (black dots), and 8° (gray diamonds).

2.5. Results

Gathering the Equations (4), (5), and (11), we solve the equations in three cases, respectively:

(1) when the bending angle equals 6°, the range of f_1 is 0.401–0.443, and f_2 is 8.0–9.6,
(2) when the bending angle equals 7°, the range of f_1 is 0.396–0.436, and f_2 is 6.8–8.2,
(3) when the bending angle equals 8°, the range of f_1 is 0.391–0.429, and f_2 is 6.0–8.0.

The solutions are shown in Figure 4, and $M_1 = 1.94 - 2.29$, $V_w/c_s = 0.73 - 0.89$. Considering the sound speed of halo $c_s \sim 150 - 210$ km s^{-1} ($T = 1 - 2 \times 10^6$ K), we conclude the following.

(1) The velocity of the HGW is 110–190 km s^{-1}.
(2) The forward shock of the NPS (east part) in the frame of the GC moves with $V_{s,GC} = (M_1 - V_w/c_s)c_s = 180–290$ km s^{-1}.

We then estimate the age of the NPS by $\tau \sim d_{NPS}/V_{s,GC} = 18$–34 Myr. This is also the age of the *Fermi* bubbles.

3. Summary and Discussion

In this Letter, we estimate the age of *Fermi* bubbles/NPS based on two observational facts: (1) after the shock expansion, the NPS shows a measurable thickness, which is due to the difference in the velocities of the forward shock front and the CD; (2) both the *Fermi* bubbles and the NPS are asymmetric, with a bending angle $\theta_{bend} \approx 6°$–8°. We make an assumption that the bending may be caused by a presumed HGW blowing from east to west in Galactic coordinates, and we obtain the forward shock velocity of the NPS (east) in Galactic coordinates and the velocity of HGW. We find that the HGW's velocity is significantly lower than the unreasonably large value of 750 km s^{-1} presented in Yang et al. (2012), which may eventually strip out the gas of the Milky Way. The main reason is that, in their jet model, the forward shock is so strong that a very fast HGW is demanded to bend the bubble to the observed angle.

The existence of the HGW can be proved/disproved by absorption lines like O VII absorption lines. The Doppler shift in wavelength for the O VII Ka line (21.6 Angstrom) is 0.008–0.013 A for the velocity of 110–190 km s^{-1} in the viewing direction. However, considering the projected effect of velocity in the line of sight and the contribution of absorbers closer to the galactic plane that suffered less from the HGW, the Doppler shift is not so noticeable. This may be marginally resolved by X-ray telescope if the spectral quality is good enough (e.g., O VII absorbers for NGC 3783 in the west direction show redshift of 45–128 km s^{-1} with 1σ confidence in Gupta et al. 2012).

3.1. Comparison with Other Observational Results

We here compare our results with some observations.

(1) According to observations, the temperature of the NPS is around 0.3 keV (Kataoka et al. 2013, 2016), or 0.4–0.5 keV (Miller & Bregman 2016). If the pre-shock gas temperature is $T_0 = 0.1$–0.2 keV, the Mach number of 1.94–2.29 in our fiducial model implies that the temperature of the NPS at lower latitudes ($b \sim 20°$–30°) is around 0.2–0.46 keV, which is roughly consistent with observations.
(2) Fang & Jiang (2014) found that the shock-expansion velocity of the shocked ISM surrounding the *Fermi* bubbles is 200–300 km s^{-1}, which is roughly consistent with the result in our model.
(3) Ackermann et al. (2014) found that the gamma-ray image of Loop I (mainly coincident with, but more extended than, the NPS) is just surrounding the NFB and the lower part of the south bubble with a γ-ray photon index of $\Gamma \approx 2.4$ (see their Figure 13), implying that the power-law distribution index of the corresponding non-thermal electrons or protons is $p_{PL} \approx 2.4$. According to first-order *Fermi* acceleration theory, the Mach number of the forward shock is 3–4 (Drury 1983), which is also roughly consistent with our result.

3.2. Implications on the Fermi *Bubbles' Age*

Our model provides a novel method to estimate the age of the *Fermi* bubbles/NPS, independent of detailed dynamical and radiative models. The age is $\tau \sim 18$–34 Myr. This is roughly consistent with the $\tau_{Fermi} = 7$–12 Myr in the "hot accretion wind" model (Mou et al. 2014, 2015), $\tau_{Fermi} = 6$ Myr in the "quasar wind" model (Zubovas et al. 2011; Zubovas & Nayakshin 2012), and $\tau_{Fermi} \approx 30$ Myr in the "star-formation-driven wind+leptonic scenario" model (Sarkar et al. 2015; Sarkar 2019). However, it is much longer than the ages of $\tau_{Fermi} \approx 1$–2 Myr in the jet model (Guo & Mathews 2012; Guo et al. 2012; Yang et al. 2012, 2013), and much shorter than $10^8 - 10^9$ yr in the "star-formation-driven wind" model (Crocker & Aharonian 2011; Crocker et al. 2014).

Our result favors the "hot accretion wind" model, the "quasar wind" model, and the "star-formation-driven wind +leptonic scenario" model. But it is worth noting that the hypothesis that past nucleus activity does not change over time may have a significant impact on the final result. Numerical simulations under several typical varying activities are worthwhile in the future.

ORCID iDs

Guobin Mou ⓘ https://orcid.org/0000-0002-0092-7944

References

Ackermann, M., Albert, A., Atwood, W. B., et al. 2014, ApJ, 793, 64
Akita, M., Kataoka, J., Arimoto, M., et al. 2018, ApJ, 862, 88
Burns, J. O., Owen, F. N., & Rudnick, L. 1979, AJ, 84, 1683
Carretti, E., Crocker, R. M., Staveley-Smith, L., et al. 2013, Natur, 493, 66
Crocker, R. M., & Aharonian, F. 2011, PhRvL, 106, 101102
Crocker, R. M., Bicknell, G. V., Carretti, E., et al. 2014, ApJL, 791, L20
Crocker, R. M., Bicknell, G. V., Taylor, A. M., & Carretti, E. 2015, ApJ, 808, 107
Dobler, G., Finkbeiner, D. P., Cholis, I., et al. 2010, ApJ, 717, 825
Drury, L. O. 1983, RPPh, 46, 973
Egger, R. J., & Aschenbach, B. , 1995, A&A, 294, L25
Fang, T., & Jiang, X. 2014, ApJL, 785, L24
Ghez, A. M., Salim, S., Weinberg, N. N., et al. 2008, ApJ, 689, 1044
Guo, F., & Mathews, W. G. 2012, ApJ, 756, 181
Guo, F., Mathews, W. G., Dobler, G., & Oh, S. P. 2012, ApJ, 756, 182
Gupta, A., Mathur, S., Krongold, Y., et al. 2012, ApJL, 756, L8
Hayes, J. C., Norman, M. L., Fiedler, R. A., et al. 2006, ApJS, 165, 188
Jones, T. W., & Owen, F. N. 1979, ApJ, 234, 818
Kataoka, J., Sofue, Y., Inoue, Y., et al. 2018, Galax, 6, 27
Kataoka, J., Tahara, M., Totani, T., et al. 2013, ApJ, 779, 57
Kataoka, J., Tahara, M., Totani, T., et al. 2016, ApJ, 807, 77
Kuntz, K. D., & Snowden, S. L. 2000, ApJ, 543, 195
Lallement, R., Snowden, S., Kuntz, K. D., et al. 2016, A&A, 595, 131
Miller, M. J., & Bregman, J. N. 2013, ApJ, 770, 118
Miller, M. J., & Bregman, J. N. 2016, ApJ, 829, 9
Mou, G., Yuan, F., Bu, D., et al. 2014, ApJ, 790, 109
Mou, G., Yuan, F., Gan, Z., & Sun, M. 2015, ApJ, 811, 37
O'Donoghue, A. A., Eilek, J. A., & Owen, F. N. 1993, ApJ, 408, 428
Puspitarini, L., Lallement, R., Vergely, J.-L., & Snowden, S. L. 2014, A&A, 566, A13
Sarkar, K. C. 2019, MNRAS, 482, 4813
Sarkar, K. C., Nath, B. B., & Sharma, P. 2015, MNRAS, 453, 3827
Snowden, S. L., Egger, R., Freyberg, M. J., et al. 1997, ApJ, 485, 125
Sofue, Y. 2000, ApJ, 540, 224
Sofue, Y. 2015, MNRAS, 447, 3824
Sofue, Y., Habe, A., Kataoka, J., et al. 2016, MNRAS, 459, 108
Stone, J. M., & Norman, M. L. 1992, ApJS, 80, 753
Su, M., Slatyer, T. R., & Finkbeiner, D. P. 2010, ApJ, 724, 1044
Sun, X. H., Gaensler, B. M., Carretti, E., et al. 2014, MNRAS, 437, 2936
Totani, T. 2006, PASJ, 58, 965
Weaver, R., McCray, R., Castor, J., et al. 1977, ApJ, 218, 377
Wolleben, M. , 2007, ApJ, 664, 349
Yang, H.-Y. K., & Ruszkowski, M. 2017, ApJ, 850, 2
Yang, H.-Y. K., Ruszkowski, M., Ricker, P. M., et al. 2012, ApJ, 761, 185
Yang, H.-Y. K., Ruszkowski, M., & Zweibel, E. 2013, MNRAS, 436, 2734
Yuan, F., Gan, Z. M., Narayan, R., Sadowski, A., et al. 2015, ApJ, 804, 101
Yuan, F., & Narayan, R. 2014, ARA&A, 52, 529
Zubovas, K., King, A. R., & Nayakshin, S. 2011, MNRAS, 415, L21
Zubovas, K., & Nayakshin, S. 2012, MNRAS, 424, 666